International Journal of Impact Engineering 204 (2025) 105376

Contents lists available at ScienceDirect

International Journal of Impact Engineering

journal homepage: www.elsevier.com/locate/ijimpeng

Experimental study and modelling of shock-induced compaction of autoclaved aerated concrete through MHz X-ray radioscopy

J. Tartière [a], M. Arrigoni [a,*], B. Lukic [b], A. Rack [b], D. Chapman [c], B. Reynier [a,d], J. Le Clanche [a], P. Pradel [d], T. De Resseguier [e], P. Forquin [f], D. Eakins [c]

[a] ENSTA IPP, IRDL UMR 6027 CNRS, 29200 Brest, France
[b] European Synchrotron Radiation Facility, CS40220, 38043 Grenoble Cedex 9, France
[c] Department of Engineering Science, University of Oxford, Oxford OX1 3PJ, UK
[d] CEA CESTA, 15 avenue des Sablières CS60001, 33116 Le Barp Cedex, France
[e] Institut Pprime, UPR3346, CNRS, ISAE-ENSMA, 11 boulevard Marie et Pierre Curie, Futuroscope Chasseneuil Cedex, France
[f] University Grenoble Alpes, CNRS, Grenoble INP, 3SR, 38000 Grenoble, France

ARTICLE INFO

Keywords:
Autoclaved aerated concrete
Shock wave
Compaction
X-ray imaging
Plate impact

ABSTRACT

Extreme scenarios related to sudden increase of stress states, such as mechanical impacts or collisions, can lead to severe physical damage on structures. However, through their compaction phase, porous materials absorb a part of mechanical energy and efficiently mitigate the shock wave induced damage. Autoclaved Aerated Concrete (AAC) is one type of cellular materials which exhibits such capability and also being non-flammable, which is of interest for most structures that must resist both impacts and fire. With good insulation properties and its low density, AAC is therefore a material of choice in protective design against shock loading.

It is however difficult to study in real time, especially because of the cloud of dust produced during compaction. In the present study, two AAC of respective densities of 550 kg/m^3 and 115 kg/m^3 are considered. Plate impact tests were performed at the European Synchrotron Radiation Facility (ESRF) and the compaction process was observed *in-situ* by ultra-fast X-ray phase-contrast radioscopy for impact velocities ranging from 250 to 400 m/s.

Through the records analysis, a compaction front is identified..The tracking of the compaction front and the initial velocity of the projectile provide a portion of the AAC compacted state. In line with the findings, an extended analysis extracting the mean pore size and the evolution of the densities and speed of sounds is conducted by the use of laser induced shock waves on samples pre-compacted. An analytical model is proposed to reproduce the compaction front dynamics, considering equivalent mass-spring systems.

1. Introduction

Aeronautical and space systems constantly need to improve their mechanical performance while reducing energy consumption, in the interest of cost-effectiveness. In flight, as well as during maintenance operations, these systems can be exposed to impacts of varying severity, from falling tools to hyper-velocity impacts, for example. This range of threats calls for an adapted structural design using highly technical materials. Composite materials and structures are known to be one of the best choices due to their high mechanical strength and light weight [1]. However, they may not be sufficient to withstand severe impacts such as ballistic or micrometeorite impacts. In addition, they remain flammable and require a sophisticated implementation that can be costly. Thus, combining them with other materials, such as ceramics [2] or light metals [3,4] in the design of the structure can offer enhanced performance. However, these combinations impose a weight penalty that remains a challenge.

Porous materials may overcome the weight penalty and bring into play compaction as an active mechanism for energy absorption. Sintering and plasma spraying techniques offer the possibility of having porous metals and ceramics [5,6] for which mechanical modelling under dynamic loading can be found in the literature [7,8] but the porosity content is not significant enough to limit the weight penalty. Syntactic or expanded polymeric foams could offer an interesting areal density to

* Corresponding author.
E-mail address: michel.arrigoni@ensta.fr (M. Arrigoni).

https://doi.org/10.1016/j.ijimpeng.2025.105376
Received 26 February 2025; Received in revised form 16 April 2025; Accepted 21 April 2025
Available online 28 April 2025

energy absorption [9–11] but are flammable. Metallic foams are of interest and have been recently used in ballistic protection design [12] but remain costly. Additive manufacturing (AM) is an interesting technique to produce cellular materials with a controlled porosity [13], but manufacturing times for sufficiently large samples (> 10 mm) with small porosities (10–100 μm) are still too long. Recently, shock compression of porous carbon foams was the object of fast X-Ray experiments using the Phase Contraste Imaging (PCI) technique [14] on plate impact experiments. It allowed the construction of the Hugoniot curve with the same accuracy as that obtained with material speed measurement by Photonic Doppler Velocimetry. Among other alternative materials, Autoclaved Aerated Concretes (AAC) have an interesting potential of energy absorption [15,16], are inflammable and can be manufactured at large scale with castable possibilities. They also have a very low carbon footprint and can be easily recycled in mortars and cements [17,18]. They were elaborated in the mid-1920s in Sweden [19] and are still nowadays involved in civil engineering for their effective insulation properties.

Unfortunately, commercial use of AAC materials in protective structures has been hampered by limited information on their compaction behaviour, which has received very little attention to date. One of the first attempts was proposed by Belouettar [20] on AAC of density of 550 kg/m^3 up to a strain-rate of 10 s^{-1}, that remains insufficient for being representative of the strain-rate occurring during high velocity impacts events (> 10^4 s^{-1}). A recent study pointed out the relevance of thicker AAC wall to better resist the effects of blast loading [21]. The authors modelled their experiments using Abaqus software but without considering compaction, which was not assumed to play a major role in these experiments. A plate impact approach was followed by Mespoulet et al., [22]. They covered a large range of strain-rates from quasi-static loading to plate impact (above 10^3 s^{-1}) on 550 kg/m^3 AAC. To do so, they used direct and reverse plate impact experiments with samples of large diameter ($\varnothing$ > 70 mm) with respect to the pore size. The back-face velocity of an aluminium plate impacted with a AAC projectile was measured by Photonic Doppler Velocimetry (PDV) [23]. They obtained only one characteristic point of the compaction curve (P, ρ). They confirmed that the brittle behaviour of AAC does not allow a direct visualisation for observing the compaction during impact because of the emitted dust during AAC crushing. Liu et al., [24] studied a similar AAC with a 500 kg/m^3 density until a strain-rate of 100 s^{-1}. They evidenced that the dynamic strength of AAC material increases with strain-rate in compressive uniaxial loading but they could not observe the compaction wave. Recently, Aminou et al., [25,26] investigated the compaction of a 115 kg/m^3 AAC and evidenced its beneficial use in protective structure applications. They could propose a stress-strain measurement of this AAC and use it in a SPH model in LS-Dyna that matched well to experimentally measured out-of-plane displacement of a blasted plate having a sacrificial cladding of such AAC.

The above overview of the scientific literature points out that the AAC density of 500 kg/m^3 is popular in building construction and its behaviour under high strain-rate is difficult to investigate because of obscuration during crushing. It is noted that few relevant studies exist on the compaction of AAC by plate impact with rapid X-ray observation, even though promising approaches were carried out on compaction of granular ceramics [27] and in porous titanium [28] with Hopkinson bars.

The aim of this study is to provide such experimental data and to propose an analytical model for the prediction of the compaction wave speed in AAC materials. A methodology for a dynamic characterization, from quasi-static behaviour to compaction under shockwave, applicable to all AAC variants is proposed. To do so, two different variants of AAC were chosen from Xella manufacturer, Multipor and Siporex, of contrasted densities of 115 kg/m^3 and 550 kg/m^3 respectively. Samples were subjected to quasi-static compression tests and plate impact experiments at the ESRF facility [29,30], where dynamic compaction was observed with ultra-high X-ray radioscopy. To develop the mechanical modelling, intermediate compressed samples of various residual stiffnesses were subjected to speed of sound measurements. The analytical modelling is developed and detailed in the discussion, and finally conclusions from this work are presented.

2. Materials and methods

AAC invention is attributed to Michaelis in 1880 [31] but a manufacturing process by autoclave was patented by Ericksson in 1924 [32] to launch AAC on the construction market. The basic recipe of AAC is a mixture including: Pure white silica sand (60–70 %), Cement (15–20 %), Lime (12 to 18 %), Water, Expanding agent (<0.05 %) in mass fraction. This expanding agent is composed of aluminium that reacts completely with excess lime in aerated concrete. It transforms into aluminium hydroxide and then into tricalcium aluminates, non-volatile mineral products. Density and physical characteristics are tuned by precisely adjusting percentages and exact compositions of both materials are given in [33].

2.1. Multipor and siporex

Multipor is an ultra-light mineral foam, non-flammable with good thermal and acoustic insultation properties. Siporex is a structural AAC for building construction. Both material manufacturing induces a low carbon footprint and both a compliance with ECHA (European regulation n°1907/2006 for zero emission of chemical substances dangerous for health). Both materials are manufactured by Xella and their mechanical characteristics are given in Table 1.

A microstructural analysis by the use of optical micrographs of a flat sample plane was attempted in order to estimate the average pore size for respectively Siporex and Multipor. Although this analysis remains bidimensional, a Python subroutine could extract the contour of each pore after picture binarization with a median threshold (Fig. 1). In the picture, the area is 3160 mm^2 for Siporex (up) and 1200 mm^2 for multiport (down), the resolution is for both pictures is 8256 × 5504 pixels. The average diameter Φ_{pore} of each pore was estimated as:

$$\varnothing_{pore} = 2 * \sqrt{\frac{S}{\pi}} \quad (1)$$

where S is the average pore surface inferred from the micrograph.

The pore population was then plotted by class of size of 75 μm and the respective average diameters resulting from this analysis are 0.7 mm for Siporex and 1 mm for Multipor (Fig 2).

2.2. Compression to intermediate densities

In order to assess the sound velocity of compacted phase of Multipor and Siporex, both materials were subjected to compression in a hydraulic press at respectively 40, 80 and 160 MPa in a cylindric tube of 40 mm of inner diameter. Resulting specimens, 3 per pressing force, were extracted, measured and weighed in order to determine their densities. Results are given in Table 2.

The evolution of the density with the compaction stress is fitted with expression (2) from experimental results exhibited in Fig. 4 for each AAC

Table 1
Siporex and Mutlipor mechanical characteristics.

	Density ρ_0 (kg/m^3) dry	Young Modulus E (MPa)	Shear Modulus G (MPa)	Average pore diameter a_0 (mm)	Yield limit Y_0 compression (MPa)
Multipor [33]	115	30	–	0.792	0.35
Siporex [33]	550	2740	1096	1.047	4.5

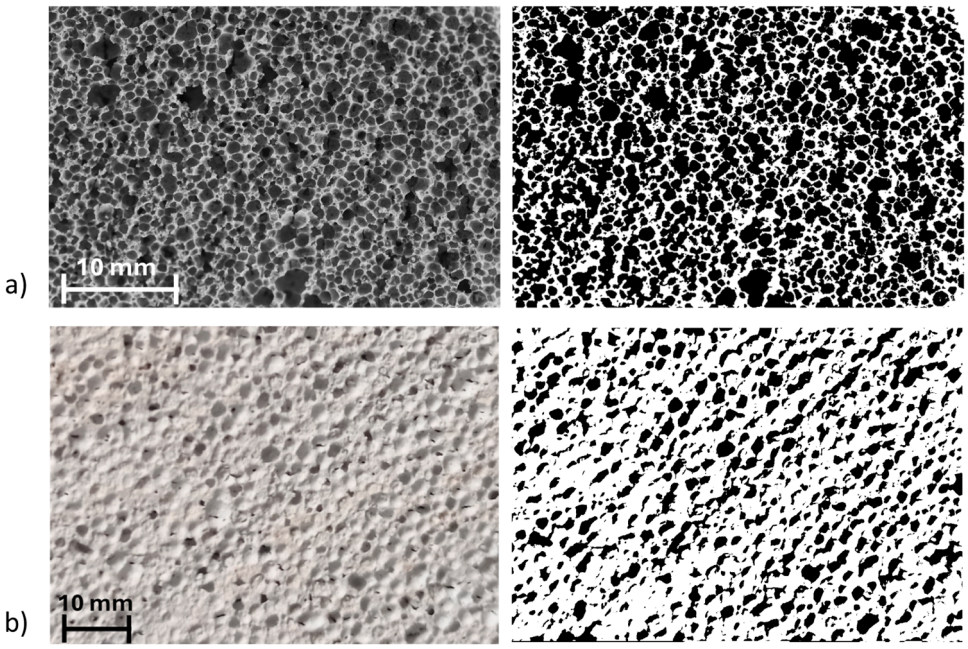

Fig. 1. Binarisation of optical micrographs of Siporex (a) and Multipor (b) for pore counting.

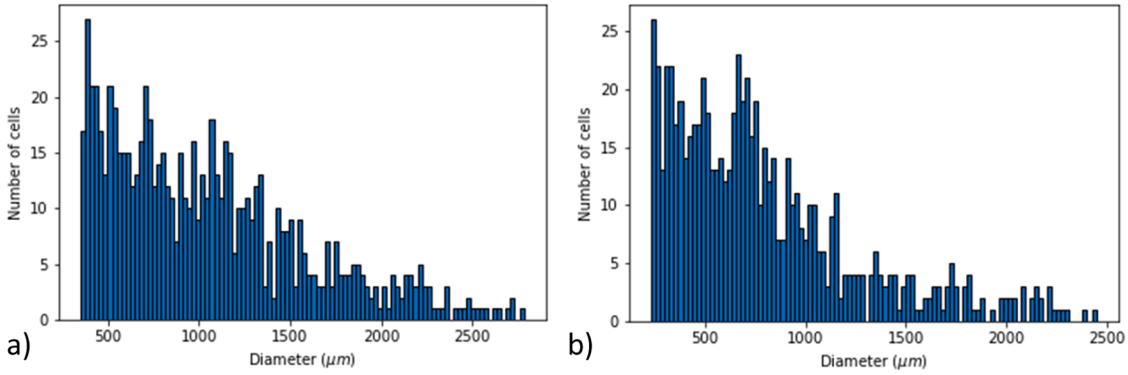

Fig. 2. Pore size distribution in a) Siporex, b) Multipor.

Table 2
Densities and speeds of sound for various compaction stage of Multipor and Siporex samples.

Compaction stress [MPa]	Multipor Density ρ [kg/m^3]	Siporex	Multipor Speed of sound C_L [m/s]	Siporex	Multipor Young Modulus E [GPa]	Siporex
0	115±5	550±5	522*	1651*	0.03	2.75
40	1025.8 ± 10	1263.3 ± 10	1654±40	1738±100	2.81	3.82
80	1111.3 ± 50	1367.6 ± 50	2023±75	1815±75	4.55	4.50
160	1266.6 ± 100	1417.4 ± 100	2537±100	1927±40	8.15	5.26

* indicates that the data is deduced from Eq. (2).

at various compaction stages:

$$\rho(P) = (\rho_c - \rho_0)\left(1 - e^{-kP}\right) + \rho_0 \quad (2)$$

with ρ_c is the critical density that is the experimental asymptotic density in the prospected range of compaction, ρ_0 is the initial density, P the hydrostatic pressure and k a constant.

2.3. Speed of sound measurement by laser driven shockwave

In order to characterise the speed of sound dependency on density for both materials, the longitudinal speed of sound was measured by laser induced compression wave [34] applied on AAC samples previously compacted to different densities.

In this experiment (Fig. 3), a thin circular plate of compacted AAC material of diameter 40 mm and thickness 3 mm is placed horizontally as a target subjected to a weak shock wave generated using the pulsed laser with the BELENOS facility at ENSTA, which is a Nd:YAG pulsed source of 1064 nm wavelength and pulse duration of 7.5 ns. The laser beam is focused in glass confinement geometry [35] on a 4 mm diameter spot in vis a vis of which a PDV system probes the free surface velocity. In order to have a better reflection of the PDV laser at the AAC back face, a 15 μm thick aluminium layer is stuck on the free surface of the compacted AAC. In order to create a better-known laser-matter interaction

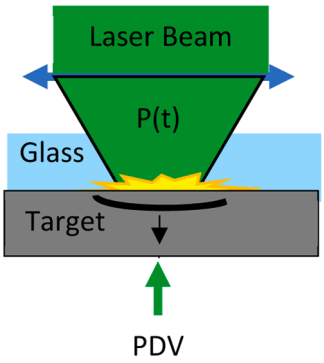

Fig. 3. Experimental setup for measuring the speed of sound in a compressed AAC sample.

and avoid water diffusion into the AAC, another 15 μm thick aluminium foil is stuck on the irradiated face too. The observed transit time then allows the estimation of the speed of sound for each compacted sample. Results are shown in Table 2. Young modulus E for each compaction stage is estimated with formula (3).

The laser driven shock experiment provides the longitudinal elastic wave speed. Actually, at the very beginning, the compression induces a shock wave but it rapidly decays to an elastic wave after propagation over some hundreds of microns beneath the loaded surface, so the mean celerity throughout the sample thickness is close to the longitudinal elastic wave speed. It was also noted that the Poisson ratio γ of the AAC is nearly null, so at the end, the speed of sound was then estimated by the use of formula (3) at a given density ρ:

$$C_L = \sqrt{\frac{E(1-\gamma)}{(1+\gamma)(1-2\gamma)\rho}} \approx \sqrt{\frac{E}{\rho}} \tag{3}$$

For the other compaction stages, uncertainties for Multipor increased with the compaction stress while decreased for Siporex.

Measured speeds of sound are also shown in Fig. 4. Speed of sound and density both exhibit a monotonic function of pressure that hardens when pressure increases and tends towards quasi-asymptotic values. Even though both matrix material of Siporex and Multipor look very similar to each other, once compacted, they point out towards different densities and speed of sound, respectively 1400 kg/m^3 and 2000 m/s for Siporex and 1250 kg/m^3 and 2500 m/s for Multipor.

2.4. Plate impacts experiments

2.4.1. Meso-scale gas launcher

The meso-scale gas launcher facility at the ESRF ID19 beamline has been used for a series of ultra-fast X-ray imaging of AAC compaction under plate impact at various impact velocities on both AAC materials. The facility, described in [29], is a single stage light gas launcher of 3 m length and of inner bore 25 mm able to reach impact speeds in the range of 200–800 m/s in an evacuated interaction chamber. It has been used successfully to study dynamic fracture in brittle materials [36,37] and the dynamics of shock interactions with spherical cavities [38]. The target material of interest is positioned within the chamber in the path of the X-ray beam offering a frame view of horizontal length of 12.8 mm by a vertical length of 8 mm, as detailed in paragraph 2.4.2 and in Fig. 5. The projectile comprises an aluminium 2024 disc of 2.493 mm thick and 24 mm diameter supported by a polycarbonate sabot. The projectile is conducted to the target that is made of an aluminium 2024 buffer of 1.006 mm thick at which the AAC sample is glued with cyanoacrylate glue, centred at the buffer's back face. The dimensions of the AAC samples are approximately of a square section of 7.5 × 7.5 mm^2 and about 20 mm long. The masses and dimensions of the projectiles and samples are given in Table 3.

2.4.2. Ultra-high speed X-ray imaging

Real-time observation of shock-induced compaction of the cellular structure of AAC was tracked through sample volume and *in-situ* utilising the single bunch X-ray imaging capabilities at the ID19 beamline of the ESRF [36,39]. The gas gun was aligned perpendicular to the oncoming X-ray radiation supplied by two axially aligned long-period undulators (λ_u=32 mm, N_u=50) located 150 m away from the sample. The incoming beam consists of an intense polychromatic spectrum with considerable flux in the domain of hard X-rays with a median energy of about 26 keV. Along the vacuum flight tube (i.e., between the source and

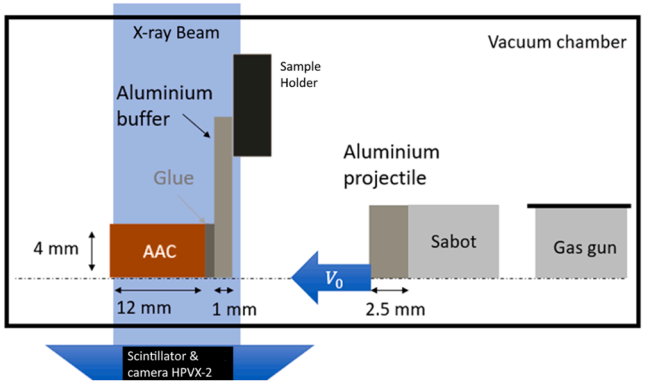

Fig. 5. Scheme of the experiment showing the AAC sample subjected to X-ray during plate impact at ID19.

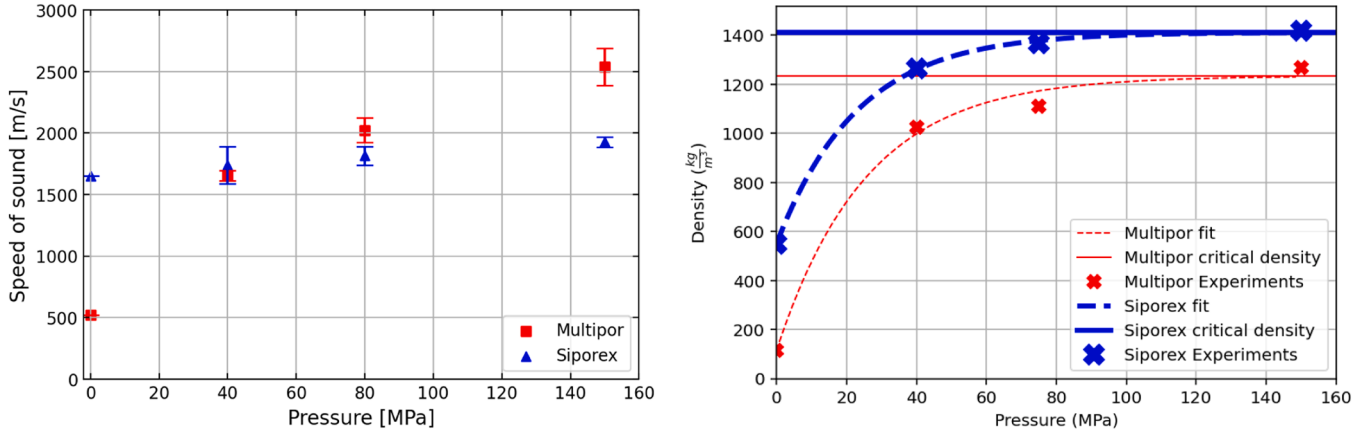

Fig. 4. Speed of sound and density evolution according to the quasi-static compression applied on the sample under hydraulic press.

Table 3
Details of Multipor and Siporex experiments at ESRF ID19.

Shot	Material	Density (kg/m^3)	Mass of sabot (g)	Impact velocity (m/s)	Thickness in Xray direction (mm)	Short name	File_name
1	Multipor®	115	18.27	250	9.44	MP1	ID19_12_33_57
2	Siporex®	550	18.31	250	8.09	S1	ID19_14_13_43
3	Multipor®	115	18.33	400	9.46	MP3	ID19_15_19_28
4	Siporex®	550	18.32	400	8.00	S2	ID19_16_23_57
5	Siporex®	550	18.33	335	6.82	S3	ID19_18_35_18
6	Multipor®	115	18.32	340	9.81	MP5	ID19_20_37_53

the sample) the beam is conditioned with two sets of slits: primary slits at 40 m away from the source for on-axis collimation and heat-load moderation, and a set of secondary slits about 135 m away from the source for collimation. Only necessary source beam filtering was employed for heat load moderation provided by permanent optical elements (i.e., 0.8 mm diamond and 2 mm beryllium windows). The ESRF operation was in the so-called 16 bunch mode where the 844.5 m circumference storage ring is populated with 16 equispaced electron-bunches (4.68 mA/bunch), providing a short X-ray illumination (i.e., 60 ps FWHM) each 176 ns. After passing through the sample, the transmitted X-ray pulse train is recorded utilising the indirect detector assembly as described in Escauriza et al., [40], positioned 9 m away from the sample. The free space propagation allows phase contrast due to (partial-)coherence of the source to form and hence enhance the visualisation of dissimilar material interfaces as well as the propagation of the dense compaction front. A pair of HPV-X2 fast framing cameras (Shimadzu, Japan) were optically relayed through pellicle beamsplitters to a 500 µm thick LYSO:Ce (Ce-dopped $Lu_{1-x}Y_xSiO_5$, Hilger Crystals, UK) single-crystal scintillator with 40 ns decay time. The visible light spectrum produced by the scintillator was collected onto the camera sensor utilising a pair of tandem Nikon 50 mm F/1.4 lenses producing an effective magnification of 1X and resulting pixel size of 32 µm/pixel. Each camera was set to an interframe time of 530 ns and effective exposure of 200 ns, capturing 128 frames of 250 × 400 pixels count in burst mode, offering a view frame window of 12.8 × 8 mm^2. The entire detector was synchronised with the pulsating storage ring radio frequency through series of trigger logic operations. The resulting configuration yielded a time sampling of 3.77 MHz and down to single bunch temporal resolution where the two-camera system captures 2 out of every 3 X-ray bunches. The instruction trigger signal was provided by the voltage drop from the velocity trap at the gas gun barrel exit, allowing for fine tuning the recorded event.

3. Results

3.1. plate impact picture analysis

Pictures are recorded with a 16 bits resolution of grey levels. For each shot, a flat field is taken after the shot, without sample. For each picture, raw pictures of the flat field are cropped by lower and upper horizontal bands of 50 pixels (Fig. 6a). Then, in the remaining central section, the grey level is averaged by pixel column and plotted along the abscissa (Fig. 6b).

By doing this grey level profile of the flat field for each picture, a space-time (*x-t, where x is the abscissa given by the pixel number in the impact direction and t is the ordinate given by the image number*) diagram

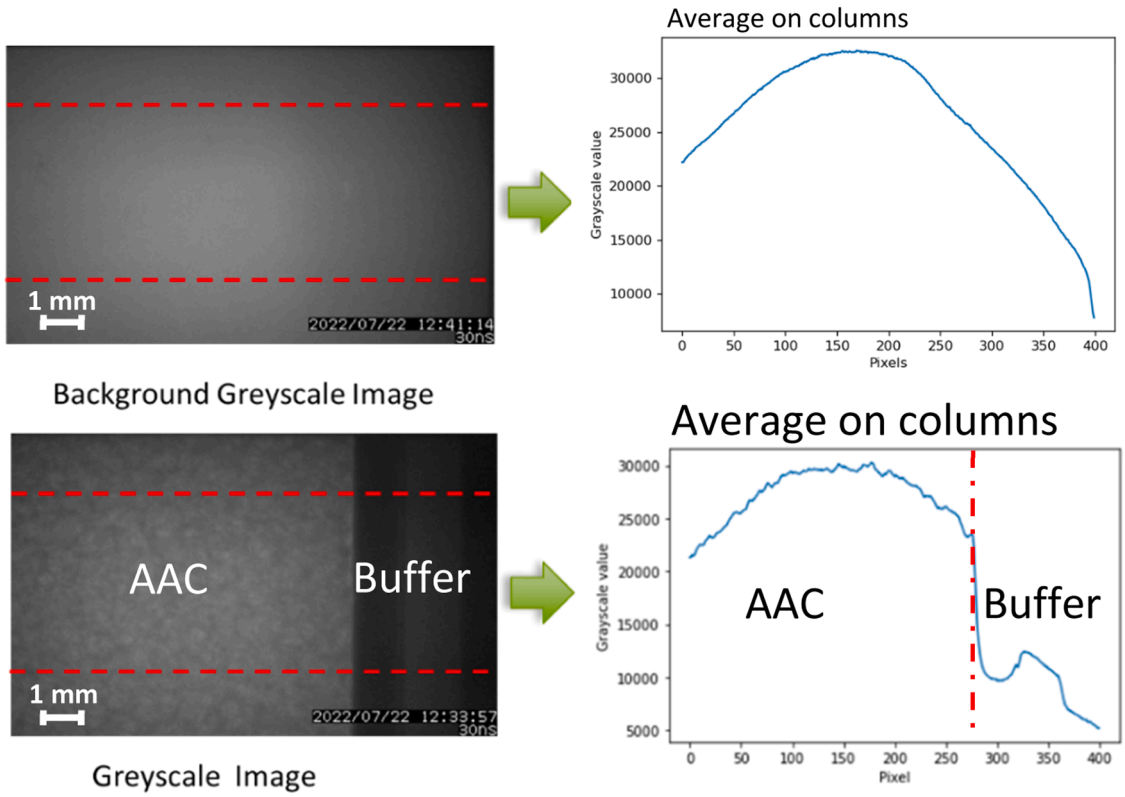

Fig. 6. a) Cropping of the flat-field picture, grey levels are averaged by column on the remaining picture and plotted along abscissa b). c) Cropping of the shot picture, grey levels are averaged by column on the remaining picture and plotted along abscissa d).

can be built representing the average scintillation of the LYSO:Ce plate during X-ray bursts during the observation time (Fig. 7a). The same operation is performed with pictures recorded during the plate impact experiment (Fig. 7b).

It can be seen in Fig. 7a that a yellow area is visible between image number 17 and 32 and between pixels columns 50 and 250, showing that the energy repartition in the X-ray beam is not homogeneous and can be evidenced as well as for the plate impact space-time diagram. The idea is to define a *x-t* matrix for the spatial and temporal correction of the pixels grey level. For the space-time diagram (Fig. 7b), a vertical dark blue band is visible around the pixel column 300, it is actually the target holder mentioned in the experimental setup. The blue oblique band corresponds to the moving projectile composed of the impacting plate and the sabot. The slope of the plate matches the impact velocity. A thin light blue stripe can be seen in this blue band, it is actually the separation of the aluminium impacting plate of the aluminium buffer plate holding the AAC sample on its opposite face. However, the gas in the barrel still pushes the sabot that pushes the flying plate against the buffer plate at about frame 45. Around that time, the left edge of this oblique blue band shows an inflection, changing its slope. In the left part between pixel column 0 and 254, an oblique line starting from frame 9 to frame 50 can be seen. It is actually the front of the compaction wave induced by the plate impact. One can see that its slope is below that of the buffer plate, meaning that the front of the compaction wave propagates faster than the buffer and impacting plates. Still in the left part, in the non-shocked media, narrow vertical stripes from instant 0 to the compaction front can be observed. They actually traduce a lack of density due to the presence of a pore.

If this analysis allows obtaining the speed of the compaction wave, it does not allow extracting quantitative density values from the grey level information since the scintillation is not homogeneous in the flat field. In order to extract densities information, a picture treatment is proposed. The first step consists in subtracting the space-time (*x-t*) picture of the plate impact to that of the flat-field averaged line by line and column by column. Then, the averaged flat-field is subtracted to the raw *x-t* picture from the shot (Fig. 8a) and normalized by its maximal value (Fig. 8b).

Then, another approach consisting in normalizing by column is tested. An (*x-t*) correction matrix is made by multiplying the grey level by either the - max or the average (two methods are tested) - of pixels values of the columns for each abscissa in the processed *x-t* picture. These two methods are respectively named “max” and “mean” and are compared in Fig. 9.

After this image flattening, the average density of the non-impacted sample can be calibrated to that of the initial density of the AAC. For each AAC an initial grey level is obtained for two respective densities of 115 kg/m^3 and 550 kg/m^3. The density calibration is performed on the *x-t* picture before normalisation in a non-shocked region of the *x-t* diagram, illustrated by a red rectangle in Fig. 9. The averaged pixels value is thus given for each shot and is equalised to the initial density of the material according to the two proposed picture treatment methods. Results are gathered in Table 4.

Having reference values for at least two different densities of AAC materials, an extrapolation of density with the grey value is proposed with the Beer-Lambert law (4)

$$I = I_0 e^{-u_m \rho t} \tag{4}$$

where I is the light intensity recorded by the camera, I_0 the light intensity of the flat field, u_m the mass-attenuation coefficient, ρ the

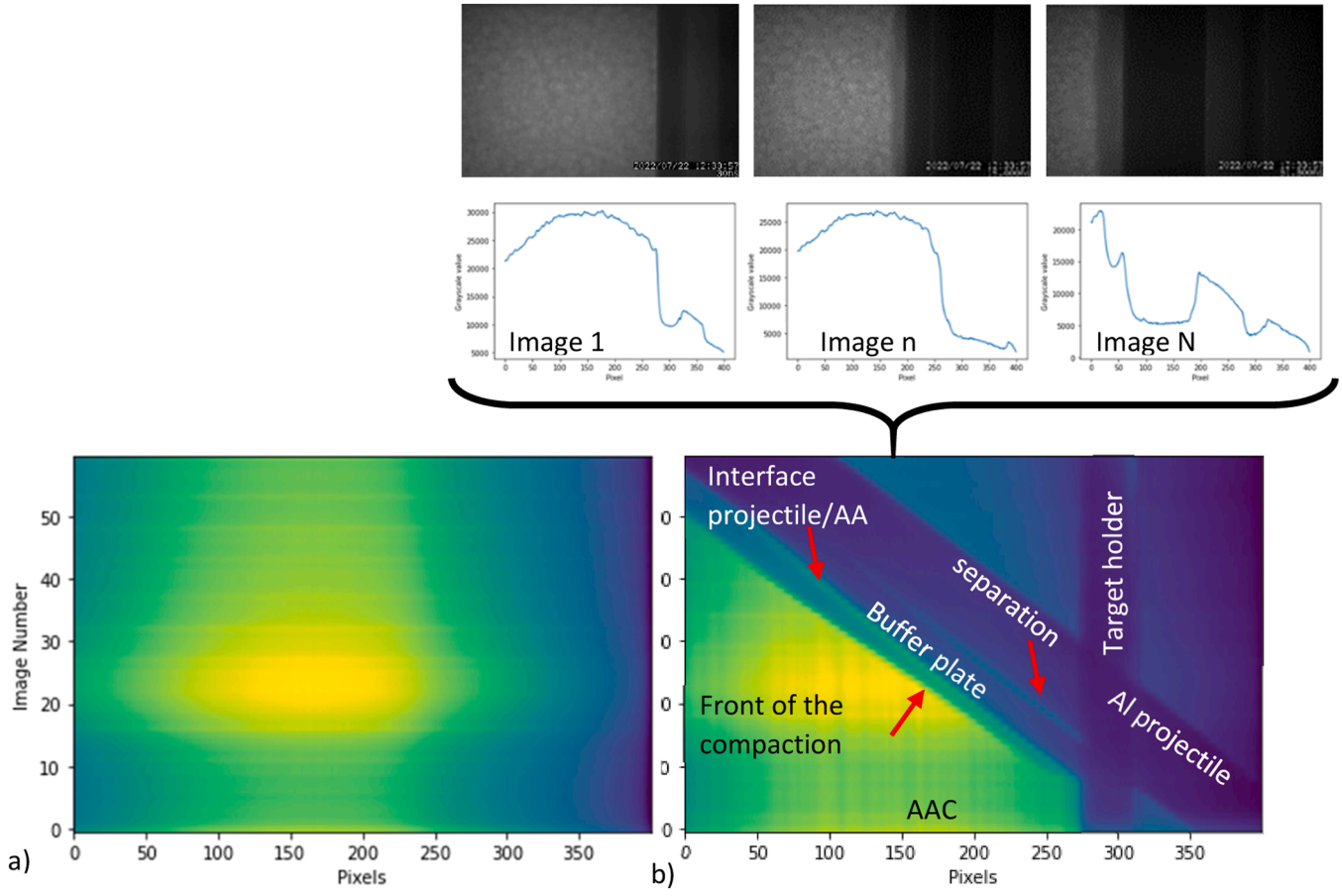

Fig. 7. example of space-time (x-t) diagram made with the picture analysis of the flat field for shot 1 in Multipor® target at 250 m/s (a) and for the plate impact experiment (b).

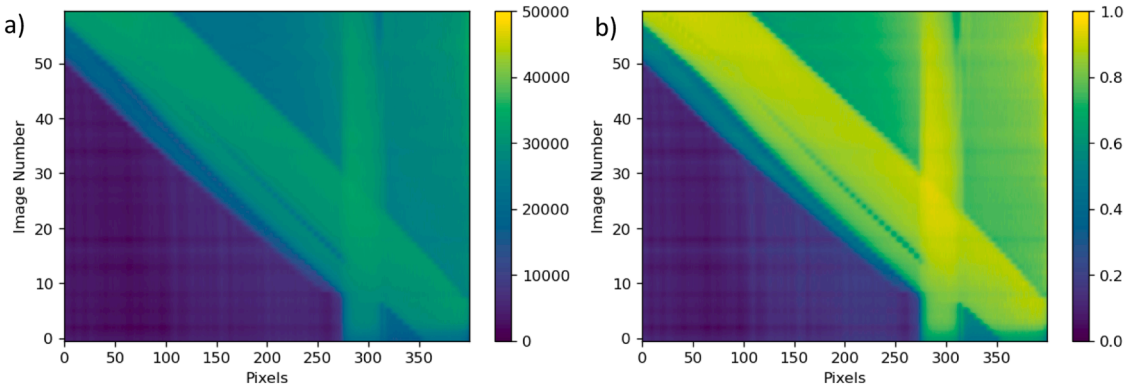

Fig. 8. a) subtraction of the x-t obtained for shot 1 in Multipor® target at 250 m/s to that of the averaged flat-field in grey scale from 0 to 65,535 (16 bits), b) Ratio the experiment x-t to the that of the flat-field, normalized.

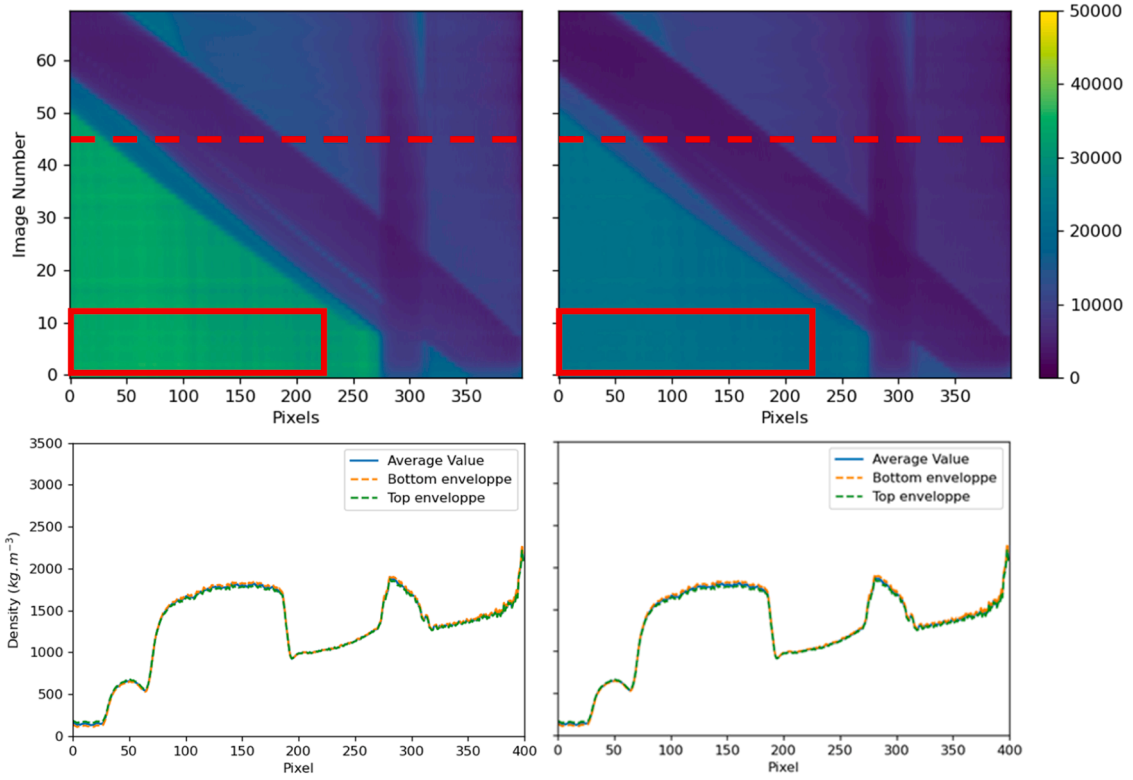

Fig. 9. Comparison between both flattening methods by max (left column) or mean (right column). The density in the target + flyer is plotted along the red dashed line (frame 45). Example taken on the *x-t* diagram of shot MP5: target Multipor® impacted at 340 m/s by a 2 mm thick Al flyer.

Table 4
Average density in "16 bits grey level" extracted from the red rectangle of the x-t diagram in non-impacted area (Fig. 9) with the "max" and "mean" flattening methods.

Flatening method	Material	Density (kg/m^3)	Sample 1	Sample 2	Sample 3	Average	Variability
« max »	Multipor®	115	4704	4552	4156	4471	±231
	Siporex®	550	10,953	11,175	9256	10,462	±857
« mean »	Multipor®	115	3187	3100	2859	3049	±139
	Siporex®	550	7509	7602	6275	7129	±605

material density and t the sample thickness crossed by the X-rays (given in Table 6).

The determination of u_m for each material is done by considering the region of interest before compaction in Fig. 9. For the materials at rest, densities ρ and light intensities I at rest and during compaction are known and shown in Tables 5 and 6, so that for each shot, an averaged u_m can be determined by using expression (4) and in Table 7. Then, knowing u_m for each sample and each material and the local light intensity I for any pixel, the density of the sample can then be estimated at any time for any pixel using Beer-Lambert law by using again relation (4).

The *x-t* correction matrix for lines and columns are then utilized in order to flatten raw *x-t* pictures. The result is given in Fig. 9 and points out that there are almost no differences. The 'max' method will be

Table 5
Intensity I extracted from x-t diagrams for the 6 shots.

Flattening method	Material	Density kg/m^3	I Sample 1	I Sample 2	I Sample 3	I Average	Variability
Max	Multipor	115	33,116	34,897	35,350	34,455	964
	Siporex	550	29,504	28,665	29,279	29,149	354
Mean	Multipor	115	22,777	23,645	24,077	23,499	541
	Siporex	550	20,227	19,499	19,850	19,859	297

Table 6
Intensities I0 for the flat-field pictures for the 6 shots.

Flattening method	Material	Density kg/m^3	I_0 Sample 1	I_0 Sample 2	I_0 Sample 3	I_0 Average	Variability
Max	Multipor	115	37,273	39,601	39,902	38,925	1175
	Siporex	550	40,457	39,841	38,536	39,611	801
Mean	Multipor	115	25,635	26,832	27,177	26,548	661
	Siporex	550	27,736	27,101	26,125	26,988	663

Table 7
mass-attenuation u_m coefficient for the 6 shots.

Flattening method	Material	Density kg/m^3	Sample 1	Sample 2	Sample 3	Average	Variability
Max	Multipor	115	0.137	0.147	0.140	0.141	0.004
	Siporex	550	0.077	0.080	0.067	0.074	0.006
Mean	Multipor	115	0.137	0.147	0.140	0.141	0.004
	Siporex	550	0.077	0.080	0.067	0.074	0.006

chosen in the analysis since it is the less costly in term of computational time.

The flattening treatment from the density x-t diagrams is applied to the shots mentioned in Table 3 and corresponding x-t diagrams after derivation and normalisation are shown in Fig. 10. Wavefronts and interfaces appear clearly. These diagrams allow a better contrast for the determination of the wave velocities visible in the x-t diagram. In this sense, local extrema are extracted and fitted with linear functions, an example is given in Fig. 11 for the impact on Multipor® at 250 m/s. This step allows the determination of the impact velocity that can be correlated with the one measured by the photodiode. The extraction of the impact speed from the x-t diagram shows a relative difference with respect of the photodiode measurement that is maximum 2 %. This speed extraction offers a good accuracy and points out the relevance of extracting the speed of the compaction wave from x-t diagram. Extracted speeds and densities are exhibited in Table 8. It can be seen that the compaction front is sharper but slower in Multipor® than in Siporex® as expected in porous materials because the higher porosity, the slower the speed of sound [41].

This analysis also reveals a visible separation, in a delimited time, between the buffer and the projectile, marked in Fig. 7 but also visible in all x-t diagrams of Fig. 10. In addition, the compaction wave does not follow a straight trajectory but exhibits a curvature that coincides with the end of the separation. The inflection in the compaction wave velocity before re-impact is due to the densification phase of porous materials during which the wave speed is slowed down due to the shape of the Hugoniot curve of the porous materials [7]. One can also notice that the very beginning of the compaction wave is not really clear, which could be attributed to the fact that the cyanoacrylate glue is absorbed in a thin layer of the AAC and makes a denser material with a wave speed higher than that of the compaction wave.

The extraction approach has been applied to all 6 x-t diagrams to obtain the average density gradient at every 5 frames (every 2.64 μs). The density profiles are plotted in Fig. 12 showing on the left column the Multipor® samples and on the right column the Siporex® samples. A first remark can be done on the fact that the compaction does not result in a clear density step. This can be the consequence of the flattening as well as the fact that pore size is not negligible with regard to the field of view of the camera. In addition, the base line before the coming of the compaction wave should be the initial density of the material at least for the first frames. Even though it is not far from this value, it is not really smooth and is even drifting. The drift could be a consequence of the propagation of a highly dispersed elastic wave in the matrix of the AAC. The oscillating base line can also be explained by the size of pores with respect to the size of the field of view. This could account for the large scatter between the average densities with minimal and maximal ones from Table 5, also visible in Fig. 9. Considering now maximal values of the density on the compaction wave, it increases with time and tends towards an asymptotic value. The density growth rate is more important in the early instant of the compaction wave propagation. This is again due to the plateau effect that follow porous materials. A second rising front, very steep that exceeds 3500 kg/m^3 is actually associated to the aluminium buffer. The order of magnitude of the density of aluminium would be expected but the grey scale calibration is made on 7.5 ± 1 mm thick AAC while the buffer is a disk of 80 mm of diameter so it is not surprising that the extracted density does not match with that of aluminium.

4. Analytical modelling

4.1. Homogenisation

The experimental data above has been used to develop a simple 1D analytical model for dynamic compaction. The motivation of developing this model is to not use mesh dependant approaches and to establish a spatial discretisation from the material microstructure. Thus, the structure of the real material is simplified according to the microstructural analysis, mechanical and geometrical data, as shown in Fig. 13 in order to obtain a 1D succession of basic elements along the impact direction, considering that then sample section remains constant during compaction.

The initial structure of the AAC material was observed by microscopy in order to extract a mean pore size l_c for both Multipor and Siporex (see Section 2.1). The total mass of the AAC sample is expressed by:

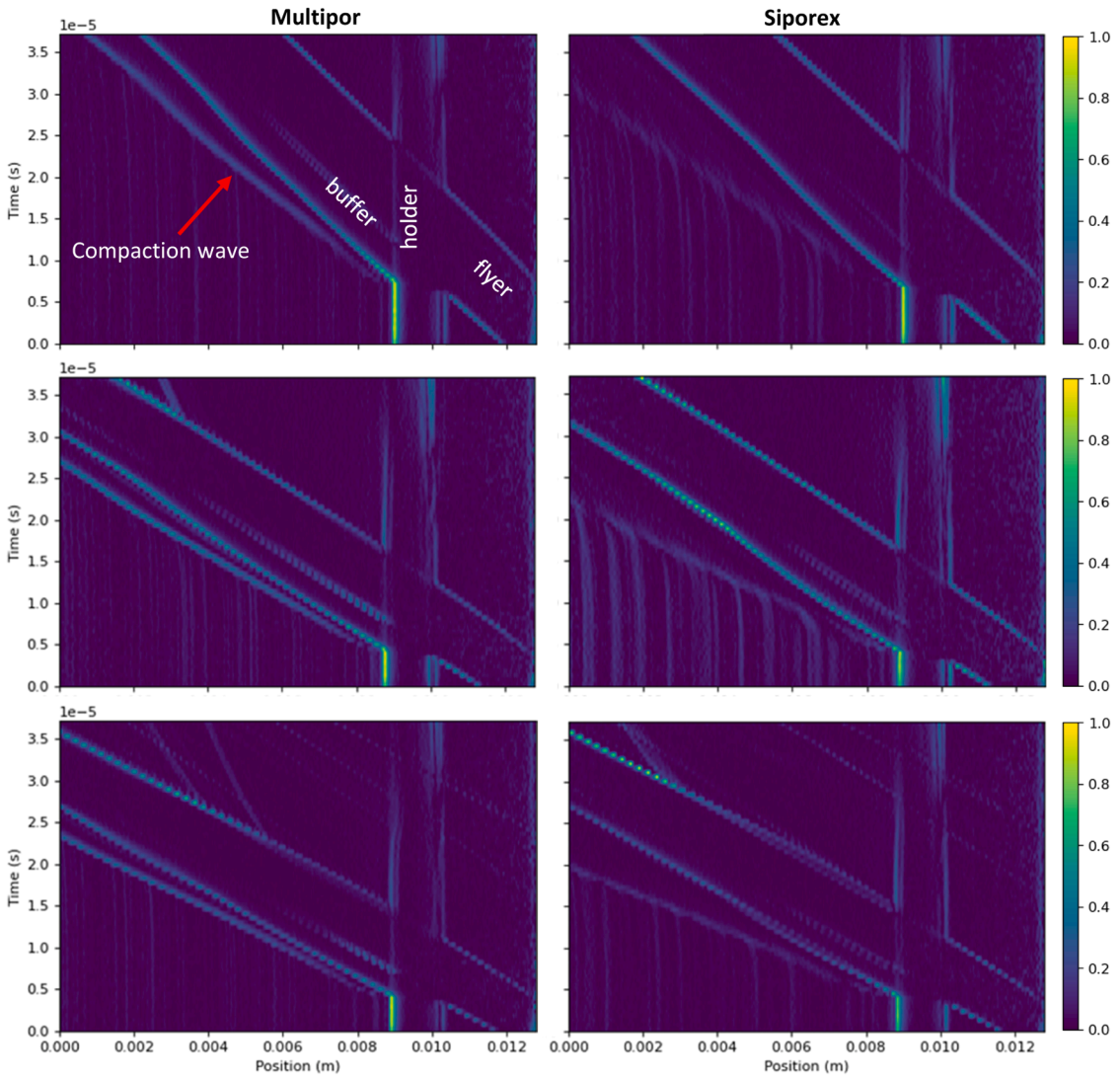

Fig. 10. x-t diagrams obtained from the Shimadzu camera after flattening. Left column shows those for Multipor® and right column for Siporex®. For the upper line, aimed impact velocities are 250 m/s, 400m/s for the middle line and 335 m/s for the last line. Interframe time is 528 ns, pixel size is 32 μm.

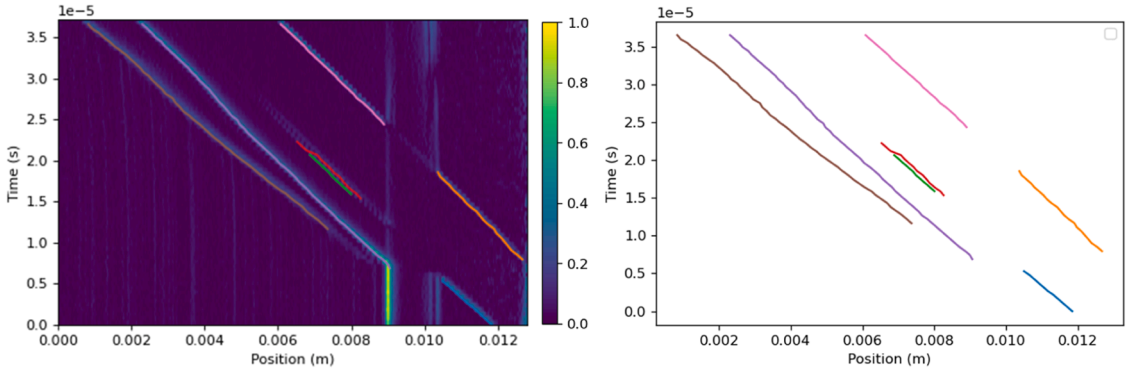

Fig. 11. Wavefront and interface tracking in shot on Multipor® at 250 m/s. Impact velocity is determined between frame 0 and 10 and is 252 m/s, very similar to that determined by photodiodes.

$$m_{total} = a^2 l_s \rho_0 \quad (5)$$

For the prepared samples the following values are considered: $a = 7.5 \pm 0.2$ mm and $l_s = 20 \pm 1$ mm.

By assuming all layers of same size and mass, the AAC sample will be represented as an effective homogeneous material discretised into a column of identical elements of same volume and mass. The AAC material is composed by two phases: 1) air filled pores and 2) a mineral matrix. A geometrical consideration allows the determination of the number of cells along the sample length, that is $N = \frac{l_s}{l_c}$ but also along the

Table 8
* Maximal densities and speeds extracted from x-t diagrams between compaction wave and buffer. Densities are estimated with the conversion function (4) at frame 40 (before re-impact).

Shot name	Material	Initial density (kg/m^3)	density * (kg/m^3)	Compaction wave speed* (m/s)	Impact velocity * (m/s)	Impact vel from diodes (m/s)	Thickness in X-ray direction (mm)	File_name
MP1	Multipor®	115	575	260	252	250	9.44	ID19_12_33_57
S1	Siporex®	550	1384	363	248	250	8.09	ID19_14_13_43
MP3	Multipor®	115	679	429	392	400	9.46	ID19_15_19_28
S2	Siporex®	550	1698	550	393	400	8.00	ID19_16_23_57
S3	Siporex®	550	1428	499	340	335	6.82	ID19_18_35_18
MP5	Multipor®	115	705	371	333	340	9.81	ID19_20_37_53

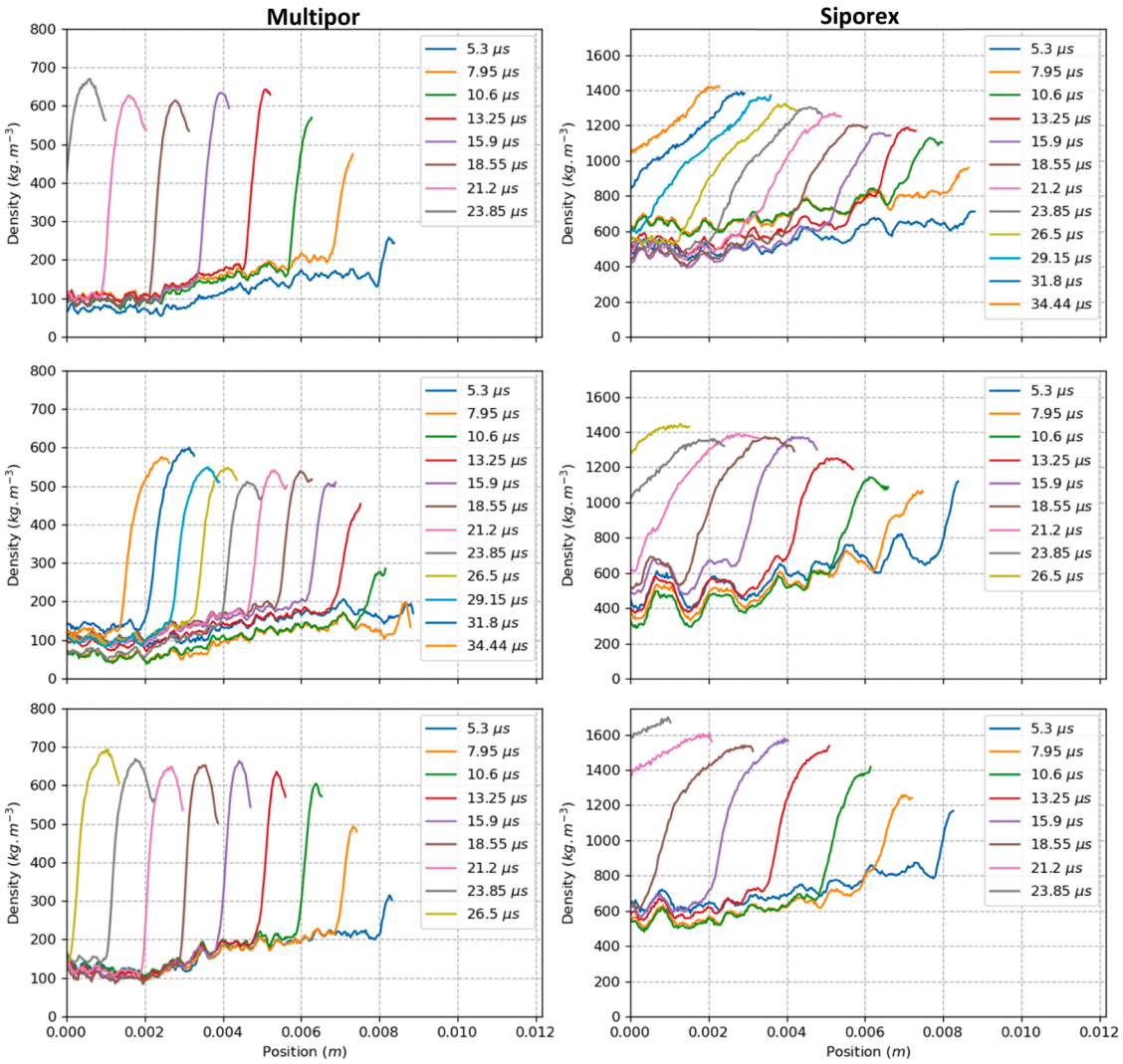

Fig. 12. Average density evolution in AAC sample along time. Left column is for Multipor sample, right column for Siporex one. Impact velocities for upper line: 240 m/s, middle line 340 m/s, bottom line 400 m/s.

edge of the sample section, leading to a total number of cells $N_{total} = \frac{l_s}{l_c}\left(\frac{a}{l_c}\right)^2$.

Thus, the single cell mass can be expressed as: $m_{cell} = \frac{m_{total}}{N_{total}}$.

4.2. Moving spring model

The proposed approach considers a uniaxial deformation of the AAC sample. A 1D analytical elementary model inspired from the Elastic-Perfectly-Plastic- (E-P-P-H) model [42] is used and presented in Fig. 14. It considers the cell during compaction, that is to say the layer of material in between the compacted and the uncompacted part of the porous material, as a spring of given stiffness k and elementary mass m_i.

The initial state of the sample is composed of a succession of as many cells as pores in the total sample length l_s. The initial length l_0 of each cell is equal to the mean pore size of the AAC sample determined in Section 2.1. The first layer of cell (thus the spring) is supposed to have a stiffness k. This assumes that the specimen consists of successive homogeneous layers of the same size of cellular concrete cells (Fig 15).

In the E-P-P-H model, three different phases for the material are

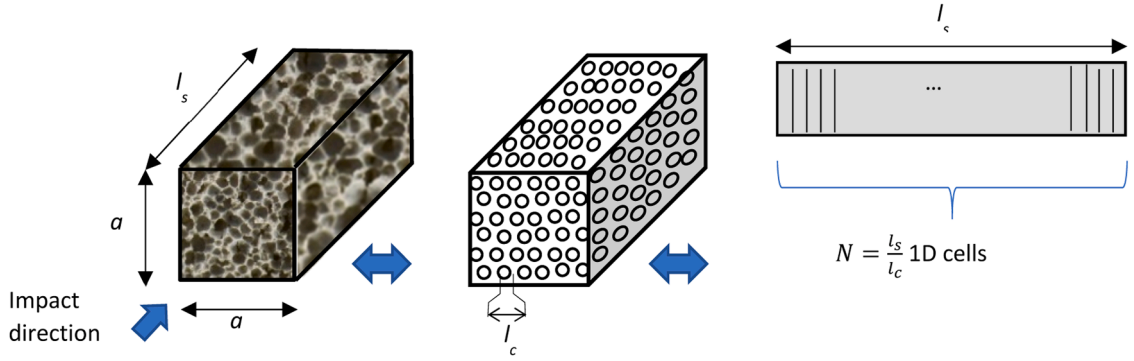

Fig. 13. Schematic of the homogenisation and simplification of a complex porous material into a simplified 1D succession of volume elements.

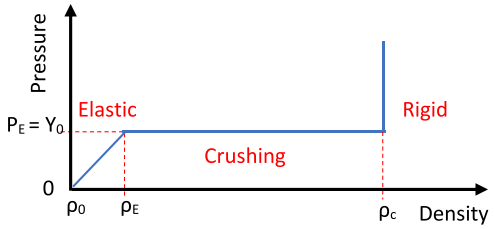

Fig. 14. Description of the Elastic-Perfectly-Plastic-Hardening approach for describing the compaction of cellular materials, inspired from [42,43].

considered and drawn in a pressure density diagram (see Fig. 14)

a reversible or elastic phase, up to an elastic pressure P_E, that is actually the yield strength of the material. The porosity is very close to the initial porosity of the material. During this elastic phase, the pressure increases linearly. Each spring is subjected to a force F_i defined by relation (8):

$$F_i = m_i\frac{dv_i}{dt} = k(l - l_0) \tag{6}$$

-An irreversible densification phase: under the effect of compression, the pores close up, the porosity decreases and thus the density increases. This densification is assumed to occur at constant pressure that is the elastic pressure P_E=Y_0. In this stage, the constant force is $F = -Y_0S$ where S is the cross-section area normal to the longitudinal direction of the sample.

-a phase of compression of the dense material: above a critical density, the compressibility drops sharply, so the pressure and force tend to become infinite and the crushing is stopped. The critical density values will be the ρc values determined for Mulipor and Siporex in Section 2.2.

-The mass of the compacted fraction of the material is then added to that of the projectile m2 and the compaction process continues in the uncompacted part. In this view, the spring is moving with the compaction wave towards the free surface of the sample and results in a mass transfer from uncompacted medium to compacted one.

- Elastic phase:

The elastic phase is governed by the harmonic oscillator Eqs. (9) and (10) applied to a cell of stiffness k placed between two masses m_1 and m_2:

$$m_1\frac{dv_1}{dt} = (l - l_0)k \tag{7}$$

$$m_2\frac{dv_2}{dt} = -(l - l_0)k \tag{8}$$

with $l = |x_2 - x_1|$ and the stiffness $k = \frac{ES}{l_0}$ with E the Young Modulus of the AAC (Table 2), S the material cross section.

By subtracting (10) by (9) and considering that $\frac{d^2(l_0)}{dt^2} = 0$ and $|x_2 - x_1| = x_2 - x_1$, one can deduce expression (11) which is a classical equation for a single spring mass system for non-null initial speed:

$$\frac{d^2(l - l_0)}{dt^2} = -\frac{k}{m_{eq}}(l - l_0) \tag{9}$$

with $m_{eq} = \frac{m_1 m_2}{m_1 + m_2}$, the initial speed being $v_l(t = 0) = v_2(t = 0) - v_1(t = 0)$ with:

$$\begin{cases} v_1(t = 0) = 0 \\ v_2(t = 0) = -v_0 \end{cases} \tag{10}$$

and the initial positions being:

$$\begin{cases} x_1(t = 0) = -l_0 \\ x_2(t = 0) = 0 \end{cases} \tag{11}$$

where v_0 is the impact velocity.

The typical solution is given by Eqs. (14):

$$l(t) - l_0 = \frac{v_0}{\omega_{0eq}}\sin(\omega_{0eq}t) \tag{12}$$

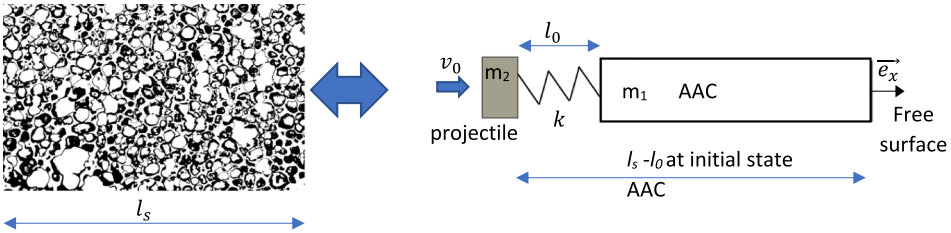

Fig. 15. Schematic description of the AAC by a series of spring-mass which initial length l_0 is equal to the mean pore diameter and stiffness equal to that of pore wall (AAC compacted).

with $\omega_{0eq} = \sqrt{\frac{k}{m_{eq}}}$ the natural frequency of the equivalent spring mass system.

Thus, Eqs. (9) and (10) can be written as Eqs. (15) and (16):

$$\frac{dv_1}{dt} = v_0 \frac{\omega_{01}^2}{\omega_{0eq}} \sin(\omega_{0eq} t) \tag{13}$$

$$\frac{dv_2}{dt} = -v_0 \frac{\omega_{02}^2}{\omega_{0eq}} \sin(\omega_{0eq} t) \tag{14}$$

with $\omega_{01} = \sqrt{\frac{k}{m_1}}$ and $\omega_{02} = \sqrt{\frac{k}{m_2}}$ that are integrated in (14–17) as expressions of respective mass m_1 and mass m_2 for respectively speed and position, using (12) and (13):

$$v_1 = -v_0 \frac{\omega_{01}^2}{\omega_{0ea}^2} \cos(\omega_{0eq} t) + v_0 \frac{\omega_{01}}{\omega_{0eq}} \tag{15}$$

$$v_2 = v_0 \frac{\omega_{02}^2}{\omega_{0ea}^2} \cos(\omega_0 t) - v_0 \left(\frac{\omega_{02}}{\omega_{0eq}} + 1 \right) \tag{16}$$

$$x_1 = -\frac{v_0}{\omega_{0ea}^3} \sin(\omega_0 t) + v_0 \frac{\omega_{01}}{\omega_{0eq}} t - l_0 \tag{17}$$

$$x_2 = \frac{v_0}{\omega_{0ea}^3} \sin(\omega_0 t) - v_0 \left(\frac{\omega_{02}}{\omega_{0eq}} + 1 \right) t \tag{18}$$

The elastic phase ends when the elongation of the spring mass system is equal to the yield strain of the AAC material.

- For the crushing phase:

In this phase, the projectile mass m_2 is completed with the compacted mass of AAC (Fig. 16). The mass m_1 of the AAC at initial state is also reduced by the compacted slice transferred to the projectile. Movement equations can thus be written as (21) and (22):

$$m_1 \frac{dv_1}{dt} = -Y_0 S \tag{19}$$

$$m_2 \frac{dv_2}{dt} = Y_0 S \tag{20}$$

The speed and displacement are then deduced by integration:

$$\frac{dx_1}{dt} = -\frac{Y_0 S}{m_1} t + v_{10} \tag{21}$$

$$\frac{dx_2}{dt} = \frac{Y_0 S}{m_2} t + v_{20} \tag{22}$$

$$x_1 = -\frac{Y_0 S}{m_1} \frac{t^2}{2} + v_{10} t + x_{10} \tag{23}$$

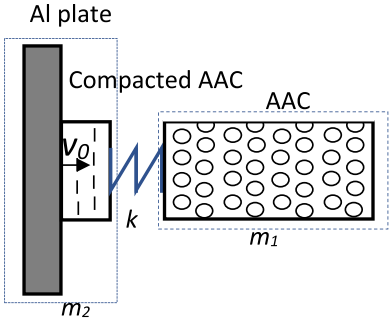

Fig. 16. Crushing stage of the AAC sample under plate impact.

$$x_2 = \frac{Y_0 S}{m_2} \frac{t^2}{2} + v_{20} t + x_{20} \tag{24}$$

For the first iteration: $x_{10} = 0$ and $x_{20} = x_{10} + l_c$ are the initial positions of respective masses m_1 and m_2. $v_{10} = v_0$ and $v_{20} = 0$ are the initial velocities of respective masses m_1 and m_2.

For the next iteration, v_{20} is the average speed of the mass m_2 at the end of the previous iteration.

4.3. Comparison with experiments

The presented moving spring model is used for computing the compaction wave evolution for each experiment. Results are matched with their respective *x-t* diagrams in Fig. 17 in which the buffer front face and the compaction wave are plotted in Fig. 17. For the compaction front, three lines are plotted, one is the compaction front computed with the average density (white dashed line) of the AAP, then the compaction front is computed with the variability of density determined from Table 8 and Eq. (6): the lower limit is plotted in cyan dashed line and the upper one in green dashed line. It does not make a noticeable difference for Multipor® (Fig. 17, left column) since the variability in grey scale is narrower than that for Siporex®. It is observed that the proposed model fits fairly well the *x-t* diagram from experiments, at least until the re-impact that is not considered by the model.

A comparison of deduced compaction wave speeds with average and lowest densities with respect to that extracted from *x-t* diagrams is given in Table 9. The model using the lower limits of the densities provides a good agreement (<5.8 %) with respect to the *x-t* diagram showing that the proposed approach can be considered as predictive.

5. Conclusion

This study aimed to develop an analytical predictive model of the dynamic compaction of autoclaved aerated concretes (AAC), leveraging physical parameters derived from new experimental observations. Historically, the inability to observe rapid events through the volume of these materials posed significant challenges. This limitation was addressed through the advent of ultra-fast X-ray imaging offered by synchrotron radiation at the ID19 beamline of the ESRF, marking a pivotal advancement in this field. Two commercially available AAC, Siporex® and Multipor®, with initial density of 550 kg/m^3 and 115 kg/m^3, respectively, were selected for investigating their compaction process under shock. AAC materials were subjected at three impact velocities: approximately 250 m/s, 340 m/s and 400 m/s. Frames captured by the ultra-high-speed X-ray detector were used to construct the space-time (*x-t*) diagrams after a suitable image calibration that was elucidate in this work. This treatment allowed the direct through-thickness visualisation of the propagating compaction front. The derivative of the flattened images highlighted wave fronts and interfaces, enabling the determination of compaction wave speed and interface velocity.

Comprehensive physical characterisation was carried out in order to obtain physical parameters that were used for derivation of an analytical model for these materials under shock loading. In addition, optical microscopy and image analysis facilitated the assessment of mean porosity size in both materials. Quasi-static compactions using a hydraulic press were performed on AAC samples in order to obtain samples at varying compaction levels. Measurements of density through weighing and sound velocity through laser-induced shock waves, enabled the derivation of an explicit relation of density and sound velocity to compaction pressure. These relationships formed the foundation of an analytical model, represented as a moving spring-mass system to describe the compaction front.

The density profiles under the plate impact exhibited a monotonically increasing trend, closely mirroring the quasi-static results and confirming the model's reliability. One of the difficulties of this

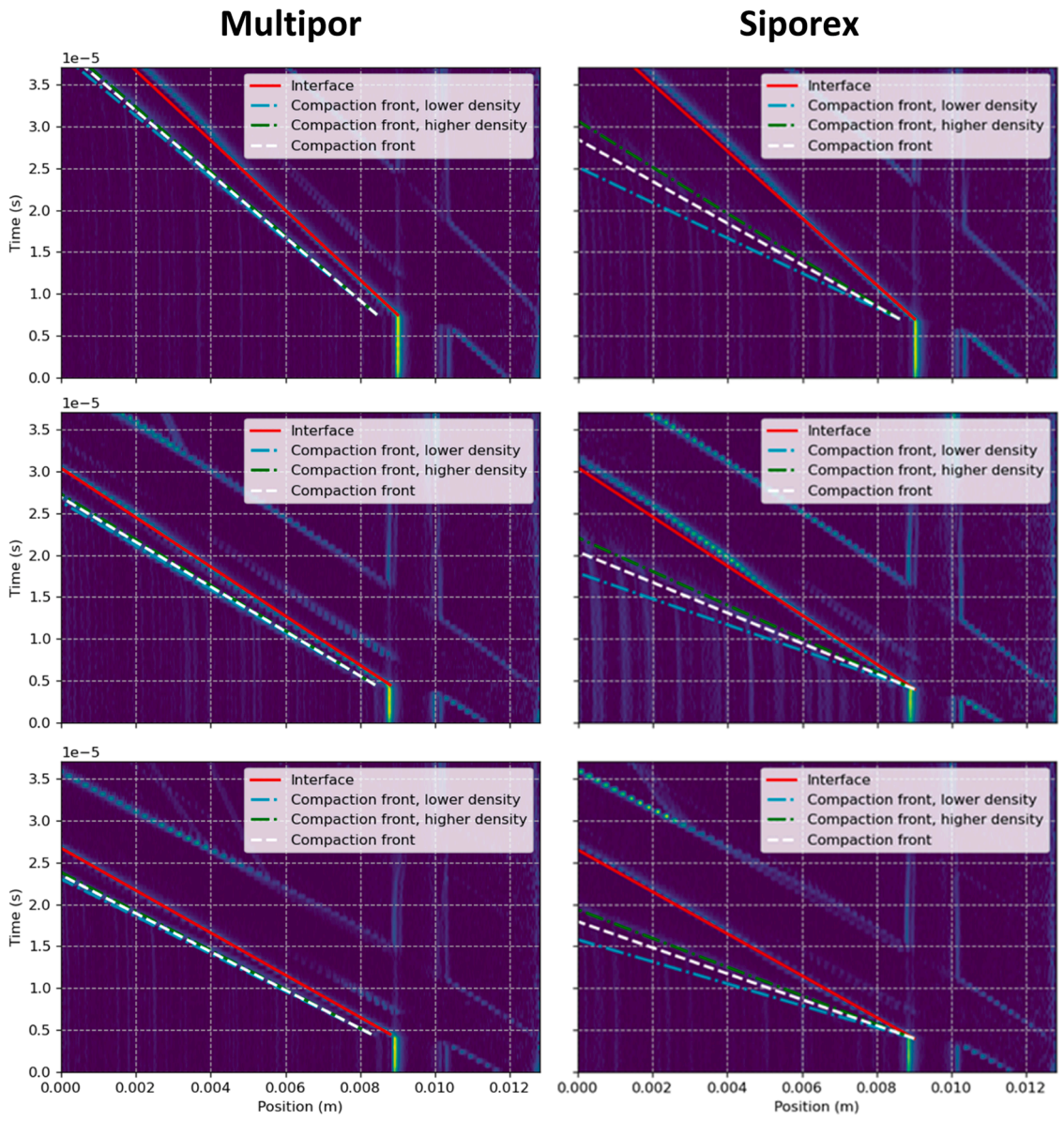

Fig. 17. Left column Multipor, with striking velocities of 250, 340 and 400 m/s, right column Siporex with striking velocities of 250, 335 and 400 m/s.

Table 9
Comparison of compaction wave speeds obtained from x-t diagram and with the model using average density or lowest density. The relative difference is given with respect to the compaction speed from the x-t diagram.

Shot name	impact speed (m/s)	compaction wave from *x-t* (m/s)	compaction wave, average (m/s)	% rel	compaction wave low density (m/s)	%rel
MP1	250	260	264	1.5	262	0.8
MP5	340	371	371	0.0	369	−0.5
MP3	400	429	429	0.0	427	−0.5
S1	250	363	401	10.5	364	0.3
S3	335	499	548	9.8	496	−0.6
S2	400	550	636	15.6	582	5.8

approach was the evaluation of the dispersion of the measured density, particularly for the case of Siporex®. While the comparison of the analytical model using an average density with the experimental results in term of compaction wave speed exhibited good agreement for Multipor®, discrepancies emerged for Siporex®. However, incorporating the lowest density within uncertainty bounds improved the alignment and rendered good agreement for both materials.

CRediT authorship contribution statement

J. Tartière: Formal analysis, Data curation, Conceptualization. **M. Arrigoni:** Writing – original draft, Supervision, Project administration, Investigation, Data curation, Conceptualization. **B. Lukic:** Supervision, Methodology, Formal analysis. **A. Rack:** Supervision, Resources, Methodology, Formal analysis. **D. Chapman:** Supervision, Resources, Methodology. **B. Reynier:** Investigation, Data curation. **J. Le Clanche:** Resources, Investigation. **P. Pradel:** Writing – review & editing, Investigation, Formal analysis. **T. De Resseguier:** Writing – review & editing, Resources, Formal analysis. **P. Forquin:** Writing – review & editing, Supervision, Resources, Formal analysis. **D. Eakins:** Writing – review & editing, Supervision, Project administration, Funding acquisition, Formal analysis, Conceptualization.

Declaration of competing interest

The authors declare the following financial interests/personal relationships which may be considered as potential competing interests:

Michel Arrigoni reports financial support, administrative support, and equipment, drugs, or supplies were provided by ENSTA, IRDL. Michel Arrigoni reports a relationship with ENSTA, IRDL that includes: employment and travel reimbursement. If there are other authors, they declare that they have no known competing financial interests or personal relationships that could have appeared to influence the work reported in this paper.

Acknowledgements

Authors would like to thank Vincent Senecloze from Xella, France for providing information on AAC and for the visit of the production site at Saint-Savin, France. Authors also thank the Shock Beam Allocation Group of ESRF for having accepted 24 hours of beam allocation on ID19.

Data availability

Data will be made available on request.

References

[1] Zhu L, Li N, Childs PRN. Light-weighting in aerospace component and system design. Propulsion Power Res 2018;7(2):103–19.
[2] Yadav S, Ravichandran G. Penetration resistance of laminated ceramic/polymer structures. Int J Impact Eng 2003;28(5):557–74.
[3] Jacques N, Barthélémy R. An analytical expression for the Hugoniot stress–strain curve of elastic-plastic cellular materials. Int J Impact Eng 2018;115:76–80.
[4] Jaulin V, Chevalier JM, Arrigoni M, Lescoute E. Characterization of a carbon fiber composite material for space applications under high strains and stresses: modeling and validation by experiments. J. Appl. Phys. 2020;128(19).
[5] L. Brémaud, J. Girardot, F. Malaise, J.-L. Zinszner, P. Forquin, I. Iordanoff, *Simulations numériques d'essais d'écaillage avec la Méthode des Élements Discrets (MED)*, CSMA 2022.
[6] V. Longchamp, J. Girardot, D. André, F. Malaise, I. Iordanoff, *Modélisation 3D par élément discret de céramiques projetées plasma à l'échelle de la porosité sous sollicitation dynamique*, CSMA 2022.
[7] Arrigoni M, Boustie M, De Resseguier T, Pons F, He HL, Seaman L, Jeandin M. Use of a macroscopic model for describing the effects of porosity on shock wave propagation. J Appl Phys 2007;(8):101.
[8] Caroll MM, Holt AC. Static and dynamic pore-collapse relations for ductile porous solids. Jnl. Appl. Phys. 1972;44:1626.
[9] Gibson LJ, Ashby MF. Cellular solids structure and properties. Cambridge Solid State Science Series. 2nd ed. Cambridge University Press; 1997.
[10] Pradel P, Malaise F, de Rességuier T. Laser-driven shock experiments to investigate mitigation ability of polymeric foams. EPJ Web Conf 2018;183:01045.
[11] Pradel P, de Rességuier T, Malaise F, Olbinado MP, Rack A, Grenzer J, Loison D, Berthe L. In situ *radiographic and ex situ tomographic investigation of pore collapse in laser shockloaded polyurethane foam*. J Appl Phys 2022;131:055106.
[12] Rabiei Marx. Ballistic performance of composite metal foam against large caliber threats. Compos Struct 2019;224:111032. 2019.
[13] Barraud E, de Rességuier T, Baillargeat J, Hemery S, Cormier J. Dynamic response of wrought and additively manufactured nickel-based alloys to high velocity impacts of laser-launched flyers. J Appl Phys 2022;131:225105.
[14] Dattelbaum DM, MacNider BC, Huber RC, Lang JM. Shock compression of a low-density carbon foam. Mater Lett 2024;360:135991.
[15] Feng S, Zhou Y, Wang Y, Lei M. Experimental research on the dynamic mechanical properties and damage characteristics of lightweight foamed concrete under impact loading. Int J Impact Eng 2020;140:103558.
[16] Nian W, Subramaniam KV, Andreopoulos Y. Experimental investigation on blast response of cellular concrete. Int J Impact Eng 2016;96:105–15.
[17] Qin L, Gao X. Recycling of waste autoclaved aerated concrete powder in Portland cement by accelerated carbonation. Waste Manage (Oxford) 2019;89:254–64.
[18] Volk R, Steins JJ, Kreft O, Schultmann F. Life cycle assessment of post-demolition autoclaved aerated concrete (AAC) recycling options. Resour Conserv Recycl 2023;188:106716.
[19] van Boggelen W. History of Autoclaved Aerated Concrete the short story of a long lasting building material. Aircrete Europe 2014.
[20] Belouettar R, Klepaczko JR, Abadlia MT. Etude du comportement mécanique du béton cellulaire autoclavé: influence de la vitesse de déformation. Revue Française de génie civil 2001;5(5):667–75.
[21] Mollaei S, et al. Investigation of behavior of masonry walls constructed with autoclaved aerated concrete blocks under blast loading. Appl Sci 2022;12(17):8725.
[22] Mespoulet J, et al. Strain rate sensitivity of autoclaved aerated concrete from quasi-static regime to shock loading. In: EPJ Web of Conferences. 94. EDP Sciences; 2015, 01053.
[23] Strand OT, Goosman DR, Martinez C, Whitworth TL, Kuhlow WW. Compact system for high-speed velocimetry using heterodyne techniques. Rev Sci Instrum 2006;77:083108.
[24] Liu C, Hou J, Hao Y, Hao H, Meng X. Effect of high strain rate and confinement on the compressive properties of autoclaved aerated concrete. Int J Impact Eng 2021;156:103943.
[25] Aminou A, Belkassem B, Atoui O, Pyl L, Lecompte D. Numerical modeling of brittle mineral foam in a sacrificial cladding under blast loading. Mech Ind 2023;24:27.
[26] Aminou A, Ben Rhouma M, Belkassem B, Ousji H, Pyl L, Lecompte D. Experimental and numerical evaluation of calcium-silicate-based mineral foam for blast mitigation. Appl Sci 2024;14(21):9656.
[27] Huang JY, Lu L, Fan D, Sun T, Fezzaa K, Xu SL, Luo SN. Heterogeneity in deformation of granular ceramics under dynamic loading. Scr Mater 2016;111:114–8.
[28] Zhao JH, Xie ZL, Zhong T, Sun T, Fezzaa K, Cai Y, Luo SN. Strain rate effects on the mechanical behavior of porous titanium with different pore sizes. Mater Sci Eng: A 2021;821:141593.
[29] Rack A, Lukić B, Chapman DJ, Strucka J, Yao Y, Mughal K, Eakins DE. Dynamic loading platforms coupled to ultra-high speed X-ray imaging at beamline ID19 of the European Synchrotron ESRF. High Press Res 2024;44(3):400–17.
[30] Rutherford ME, Chapman DJ, Derrick JG, Patten JR, Bland PA, Rack A, Eakins DE. Probing the early stages of shock-induced chondritic meteorite formation at the mesoscale. Sci Rep 2017;7(1):45206.
[31] Hewlett P, Liska M, editors. *Lea's chemistry of cement and concrete*. Butterworth-Heinemann; 2019.
[32] Eriksson 1924, Method of manufacturing porous material from portland cement US Patent, US1819018A, 1924.
[33] Xella 2021, *Guide technique construction Gros Œuvre, Protection Coupe Feu, Ytong*, https://www.xella.co.uk/en_GB/Downloads-brochures, *consulted the 2nd of November 2024*.
[34] Alil LC, Arrigoni M, Istrate M, Kravcov A, Le Pavic J, Tahan G. Laser induced shockwave as delaminator of composite material for ballistic protection at high strain rate. In: Soft Target Protection: Theoretical Basis and Practical Measures; 2020. p. 15–33.
[35] Sollier A, Berthe L, Fabbro R. Numerical modeling of the transmission of breakdown plasma generated in water during laser shock processing. EPJ Appl. Phys. 2001;16(2):131–9.
[36] Lukić B, Blasone M, Duplan Y, Forquin P, Escauriza E, Rutherford M, Rack A. Ultra-high speed X-ray imaging of dynamic fracturing in cementitious materials under impact. In: EPJ Web of Conferences. 250. EDP Sciences; 2021, 01014.
[37] Pradel P, Malaise F, De Resseguier T, Olbinado M, Rack A, Eakins D. Fast x-ray radiography to study the dynamic compaction mechanisms in a rigid polyurethane foam under plate impact. In: AIP Conference Proceedings. 2272. AIP Publishing; 2020.
[38] Escauriza EM, et al. Collapse dynamics of spherical cavities in a solid under shock loading. Sci Rep 2020;10:8455.
[39] Olbinado MP, Just Xavier, Gelet Jean-Louis, Lhuissier Pierre, Scheel Mario, Vagovic Patrik, Sato Tokushi, Graceffa Rita, Schulz Joachim, Mancuso Adrian, Morse John, Rack Alexander. MHz frame rate hard X-ray phase-contrast imaging using synchrotron radiation. Opt Express 2017;25:13857–71.
[40] Escauriza EM, Olbinado MP, Rutherford ME, Chapman DJ, Jonsson JCZ, Rack A, Eakins DE. Ultra-high-speed indirect x-ray imaging system with versatile spatiotemporal sampling capabilities. Appl Opt 2018;57:5004.
[41] Resnyansky AD, Bourne NK. Shock-wave compression of a porous material. J Appl Phys 2004;95(4):1760–9.
[42] Harrigan JJ, Harrigan JJ, Reid SR, Seyed Yaghoubi A. The correct analysis of shocks in a cellular material. Int J Impact Eng 2010;37:918–27.
[43] Zou Z, Reid SR, Tan PJ, Li S, Harrigan JJ. Dynamic crushing of honeycombs and features of shock fronts. Int J Impact Eng 2009;36:165–76.